

Composition and origin of L5 Trojan asteroids of Mars: Insights from spectroscopy

Apostolos A. Christou^{a,*}, Galin Borisov^{a,b}, Aldo Dell'Oro^c, Alberto Cellino^d and Maxime Devogèle^e

^aArmagh Observatory and Planetarium, College Hill, BT61 9DG Armagh, United Kingdom

^bInstitute of Astronomy and NAO, 72 Tsarigradsko Chaussée Blvd., BG-1784 Sofia, Bulgaria

^cINAF - Osservatorio Astrofisico di Arcetri, Largo E. Fermi 5, I-50125, Firenze, Italy

^dINAF - Osservatorio Astrofisico di Torino, via Osservatorio 20, 10025 Pino Torinese, Italy

^eLowell Observatory, 1400 W Mars Hill RD, Flagstaff, AZ 86001, USA

ARTICLE INFO

Keywords:

Trojan asteroids, Mars
Spectrophotometry
Mineralogy
Asteroids, composition
Asteroids, surfaces

ABSTRACT

We investigate the mineralogical makeup of L5 Martian Trojan asteroids via reflectance spectroscopy, paying special attention to (101429) 1998 VF₃₁, the only L5 Trojan that does not belong to the Eureka family (Christou, 2013). We find that this asteroid most likely belongs to the Bus-Demeo S-complex, in agreement with Rivkin et al. (2007). We compare it with a variety of solar system bodies and obtain good spectral matches with Sq- or S-type asteroids, with spectra of the lunar surface and of Martian and lunar meteorites. Mixture fitting to spectral endmembers suggests a surface abundance of Mg-rich orthopyroxene and iron metal or, alternatively, a combination of plagioclase and metal with a small amount of Mg-poor orthopyroxene. The metallic component may be part of the intrinsic mineral makeup of the asteroid or an indication of extreme space weathering.

In light of our findings, we discuss a number of origin scenarios for (101429). The asteroid could be genetically related to iron-rich primitive achondrite meteorites (Rivkin et al.), may have originated as impact ejecta from Mars - a scenario proposed recently for the Eureka family asteroids (Polishook et al., 2017) - or could represent a relic fragment of the Moon's original solid crust, a possibility raised by the asteroid's close spectral similarity to areas of the lunar surface. If, on the other hand, (101429) is a relatively recent addition to the Martian Trojan clouds (Christou et al., 2020), its origin is probably traced to high-inclination asteroid families in the Inner Main Belt.

For the olivine-dominated Eureka family, we find that the two smaller asteroids in our sample are more spectrally similar to one another than to (5261) Eureka, the largest family member. Spectral profiles of these three asteroids are closely similar shortward of $\sim 0.7 \mu\text{m}$ but diverge at longer wavelengths. For the two smaller asteroids in particular, we find the spectra are virtually identical in the visible region and up to $0.8 \mu\text{m}$. We attribute spectral differences in the near-IR region to differences in either: degree of space weathering, olivine chemical composition and/or regolith grain size.

1. Introduction

Trojan asteroids orbit the Sun near the L4 and L5 Lagrangian equilibrium points 60° ahead or behind a planet along its orbit (Murray and Dermott, 1999). Only three planets in the solar system, namely Mars, Jupiter and Neptune, are attended by dynamically stable Trojans. Because of their orbital stability, these objects allow us to constrain models of the earliest stages of formation of our solar system. The few known Trojans of Mars are the only known stable population of asteroids in the terrestrial planet region. They are most likely material anchored to the Martian orbit just as the solar system architecture was reaching its final configuration (Scholl et al., 2005).

Christou (2013) found that all Mars trailing Trojans, except one, form an orbital family with (5261) Eureka as its largest member. Family members show a common, olivine-dominated composition (Rivkin et al., 2007; Lim et al., 2011; Borisov et al., 2017; Polishook et al., 2017) that is generally rare among asteroids (Sanchez et al., 2014; DeMeo et al.,

ORCID(s): 0000-0002-4516-459X (G. Borisov); 0000-0002-6509-6360 (M. Devogèle)

* Corresponding author.

E-mail addresses: Apostolos.Christou@Armagh.ac.uk (A.A. Christou), Galin.Borisov@Armagh.ac.uk (G. Borisov).

©2020 Elsevier Inc. All rights reserved. This manuscript version is made available under the CC-BY-NC-ND 4.0 license <http://creativecommons.org/licenses/by-nc-nd/4.0/>

2019). The only other known L5 Trojan is (101429) 1998 VF₃₁. Compositional information for this object is limited to single visible and near-infrared reflectance spectra (Rivkin et al., 2003, 2007) as well as an albedo/size determination from thermal infrared data (Trilling et al., 2007). These indicate a similarity to S-type asteroids, quite different from the olivine-dominated Trojans and with a high abundance of pyroxene.

Here we take a fresh look at the L5 Trojans using new observations of (101429) and a more detailed examination of recently available spectra of Eureka family asteroids. Our ultimate aim is to obtain insight on the Trojans' original parent bodies and help incorporate them into narratives of the solar system's early evolution. Our study benefits from the availability of new models (Andrews-Hanna et al., 2008; Polishook et al., 2017; Neumann et al., 2018) and of spectral databases and tools for comparing asteroids to astrophysically relevant materials and surfaces (eg DeMeo et al., 2009; Popescu et al., 2012).

Table 1

Observational circumstances for observations used in this work.

Asteroid [†]	Date	Instrument	Solar analogue [‡]	Phase angle
(101429) 1998 VF ₃₁	27 Jan 2016	XSHOOTER	HD 44594	41.5°
(101429) 1998 VF ₃₁	11 May 2005	SpeX	L102-1081, L110-361	26.2°
(385250) 2001 DH ₄₇	02 Feb 2016	XSHOOTER	HD 67010	12.5°
(311999) 2007 NS ₂	02 Mar 2016	XSHOOTER	HD 67010	27.3°
(5261) Eureka	19 May 2005	SpeX	L102-1081, L105-56	4.5°

[†] Standard stars from (Landolt, 1983) and spectral solar analogues from (Hardorp, 1978)

The paper is organised as follows: in the next Section we describe the observational data obtained for this work and the methods used to spectrally compare the asteroids to other solar system bodies and laboratory-measured materials. In Section 3 we focus on (101429) where we taxonomically rank the asteroid spectrum and search for surfaces and materials that best match its spectral characteristics. Section 4 shifts the focus of the paper to the Eureka family asteroids, highlighting spectral differences and attempting to explain them. Finally, Section 5 presents our conclusions, discusses the implications of our findings and charts out avenues for future work.

2. Methods

2.1. Observations and data reduction

Observations used in this work are summarised in Table 1. All the asteroids except Eureka were observed with X-SHOOTER (Vernet et al., 2011) at the ESO Very Large Telescope facility. Details of the data reduction for the two Eureka family members discussed in Section 4 may be found in Borisov et al. (2017). Data for (101429) 1998 VF₃₁, VF31 hereafter, was likewise obtained over the spectral range 300-2480 nm through the ultraviolet blue, visible (VIS), and near-infrared (NIR) arms of the instrument. Observations were carried out in nodding mode and reduced with the ESO Reflex pipeline version 2.6.8 (Freudling et al., 2013). The spectrum was then smoothed using a running average with wavelength steps of 5 nm in the visible and 30 nm in the NIR regions. The UVB part of the obtained spectrum was discarded because of its low S/N. Finally, the binned asteroid spectrum was divided by the spectrum of the solar analogue star, which was reduced in the same way and observed on the same night, and the obtained instrumental reflectance was normalised to unity at 550 nm. The data for Eureka and the NIR part of the VF31 spectrum - kindly provided by A. Rivkin - were obtained using the SpeX instrument in prism mode on the Infrared Telescope Facility (IRTF) on Mauna Kea, Hawaii. Details on data reduction, spectra extraction and wavelength calibration can be found in Rivkin et al. (2007) and references therein. The Rivkin NIR spectrum of VF31 was smoothed using a running average with wavelength step of 20 nm and then resampled to the same wavelength locations as our spectrum.

To produce a visible and near-infrared (NIR) spectrum of VF31 suitable for analysis, we combine the NIR spectrum from Rivkin et al. (2007) with our X-SHOOTER visible spectrum (Figure 1, top panel) to take advantage of the higher S/N in our visible spectrum and in Rivkin et al.'s NIR spectrum. We do this by rescaling Rivkin's NIR spectrum to match our visible and NIR data in the overlapping wavelength interval below 1.8 μm , using the function

$$\chi^2 = \sum_i^N \frac{(R_i - f \times R_i^{\text{Rvkn}})^2}{\sigma_i^2} \quad (1)$$

where R_i and R_i^{Rvkn} are ours and Rivkin's reflectance measurements at the i^{th} wavelength position respectively, $f \in [0.80, 1.05]$ is the scaling factor and σ_i are the measurement uncertainties. The minimum χ^2 value is achieved for a scaling factor of $f = 0.9125$, which we adopt here. The resulting composite spectrum we use for taxonomic classification and search for spectral analogues in the following Sections is presented in the bottom panel of Figure 1.

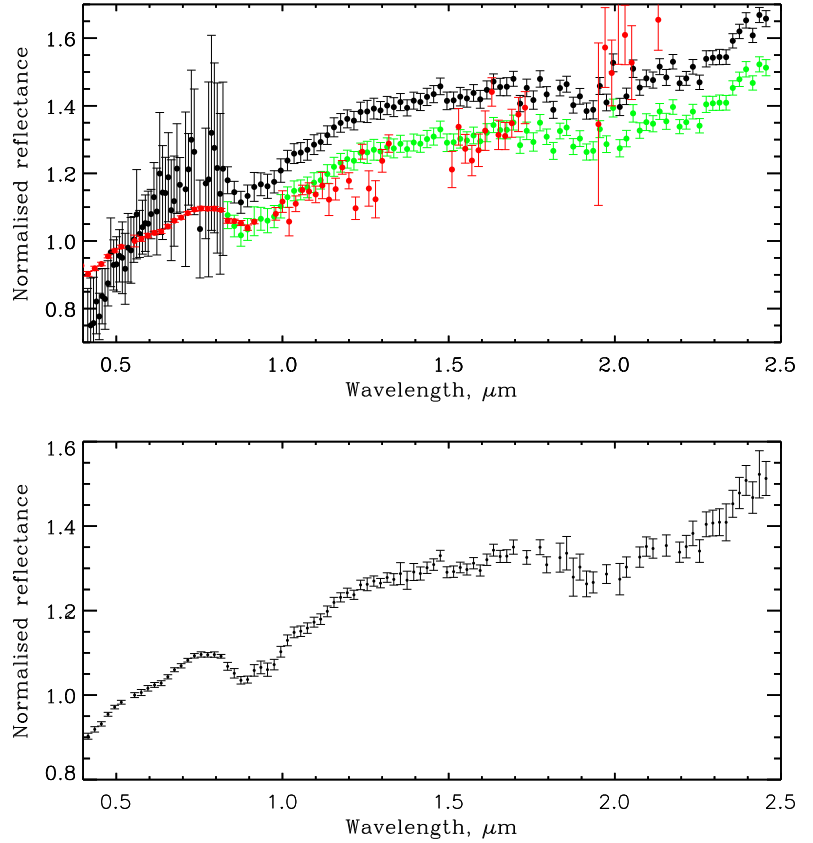


Figure 1: *Top:* The Rivkin et al. (2007) spectrum of VF31 (black), our VLT spectrum (red) and the rescaled near-infrared Rivkin et al. spectrum (green). *Bottom:* The composite VF31 spectrum used in this work.

2.2. Comparing spectra using cost functions

In the following Sections we compare the VF31 spectrum with other spectra to find the best matches. The matching procedure is based on defining suitable cost functions. If the observed spectrum i.e. the spectrum of VF31 is composed of N measurements x_i at the corresponding wavelengths λ_i , and assuming that the corresponding values μ_i of the model spectrum (i.e. other spectra) are known, the cost function measures the deviation between the two spectra. Here we use the following curve-matching cost functions (Eqs 5 and 6 resp. from Popescu et al., 2012):

$$\Phi_{\text{std}} = \frac{1}{N} \sqrt{\sum_i^N (e_i - \bar{e})^2}, \chi_\mu^2 = \sum_i^N \frac{e_i^2}{\mu_i}, \quad (2)$$

where $e_i = x_i - \mu_i$ and \bar{e} the mean value over all measurements, x_i is the measurement at the i^{th} wavelength position, and μ_i is the model evaluation at the same location. These are computationally straightforward to implement for each model spectrum and neither function depends on the measurement uncertainties. At the same time, the use of two different cost functions instead of one improves the robustness of the procedure. Note that the second of our statistical

functions is slightly modified from Eq. 6 in Popescu et al. (originally from Nedelcu et al., 2007) in that we divide by μ_i rather than x_i . For this reason, we introduce the “ μ ” subscript to distinguish between our version of the statistic and that in Popescu et al..

Given an ensemble of model spectra interpolated at the same N wavelengths λ_i as the observed spectrum, the spectra most similar to the observed spectrum are those for which the value of the cost function is lowest. In practical terms we can build a score list, one for χ_μ^2 and one for Φ_{std} , where the models are ordered by increasing value of the cost function. On the other hand, each value x_i is affected by a measurement error σ_i , and each measurement x_i is only one of the possible values coming from a statistical distribution characteristic of the measurement process. So a model could be placed at the top of the score list only by chance. Starting from some statistical assumptions about the fluctuations of the values of the observed spectrum (see Appendix A), we estimate the probability P that a particular model spectrum will be at the top of the score list.

Table 2

Taxonomic ranking of the composite spectrum of VF31.

Taxonomic class	$P_{\chi_\mu^2}$ %	Taxonomic class	$P_{\Phi_{\text{std}}}$ %
S	24.2	Xk	28.4
Xn	17.4	Xn	24.0
D	15.2	S	11.5
Xk	12.7	Cgh	9.1
L	12.5	Ch	5.9
T	7.9	L	5.2

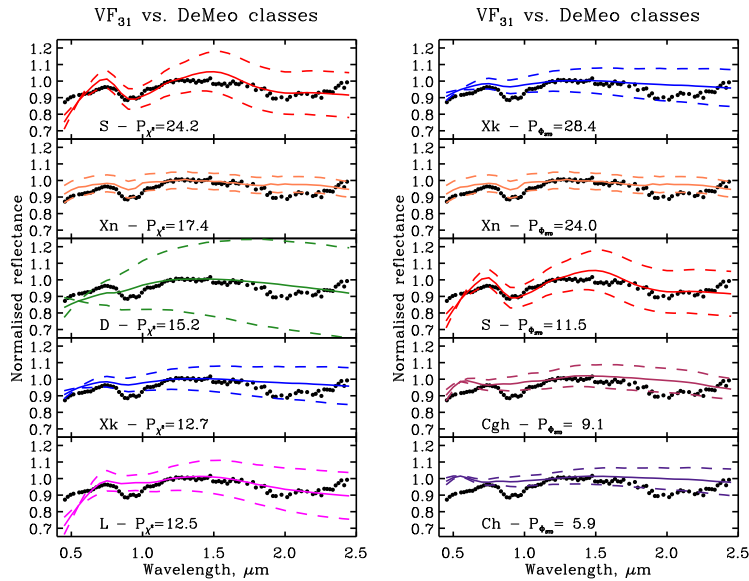


Figure 2: Visible-NIR taxonomic ranking with DeMeo average classes using χ_μ^2 (left panel) and Φ_{std} (right panel).

3. (101429) 1998 VF₃₁

3.1. Taxonomic classification

To determine the taxonomy of VF31, we compare the observed spectrum with taxonomic class average spectra from DeMeo et al. (2009) using the ranking approach described in the previous Section.

Both observed and model spectra are normalised at a common wavelength ($x_n = \mu_n = 1$ at the normalisation wavelength λ_n). We chose to normalise spectra at $\lambda_n = 1.2 \mu\text{m}$, because this position is away from absorption features at 1 and $2 \mu\text{m}$ and free from strong telluric absorption. The same choice was adopted by DeMeo et al. (2019) in their investigation of NEA spectra when only the NIR part of the spectrum was available for analysis. Finally, we remove the spectral slope before performing the match, placing more emphasis on spectral shape variations and the locations and depths of absorption features.

Table 2 lists taxonomies that scored better than $P_{\chi_\mu^2} = 3\%$ (left) and the top five hits also for $P_{\Phi_{\text{std}}}$ (right). Four out of the six taxonomic classes appear in both lists. Figure 2 shows the highest-scoring taxonomies for both the χ_μ^2 and Φ_{std} statistics. The lists include taxonomic end-members (D, L and T) which, however, do not represent the VF31 spectrum well as they are devoid of strong spectral absorptions. The same is true for primitive taxonomies in the Φ_{std} list (Cg and Cgh; not shown here). Our feature-oriented approach favours the S and Xk taxonomic classes, although Xk lacks a $2 \mu\text{m}$ absorption. S-types exhibit the same major absorption features as VF31 and, in this sense, are the best taxonomic match to the asteroid.

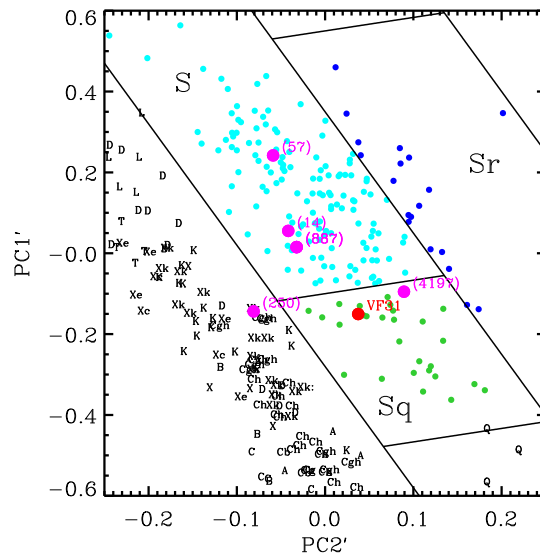


Figure 3: Location of VF31 (red point) in the PC2' vs PC1' principal component space compared to other asteroids. The 5 highest-ranked asteroids in the $P_{\chi_\mu^2}$ -sorted list (Table 3) are shown in magenta. Non S-complex asteroids are represented by black characters indicating the taxonomic class.

We complemented our ranking approach by processing the asteroid spectrum with the SMASS MIT Principal Component Analysis (PCA) software tool available online. The s/w returns, apart from the slope, the five principal components PC1' through PC5' and the Bus-DeMeo taxonomic type (DeMeo et al., 2009). VF31 plots near the Sq/S boundary in PC2' vs PC1' principal component space (Fig. 3). Sq does not appear in our P -sorted list (Table 2) but S is visually the most satisfactory fit in Figure 2, although its spectral profile variations are somewhat stronger than in the VF31 spectrum.

The SMASS tool returns a slope value of $0.2292 \mu\text{m}^{-1}$. We have reproduced this using our own fitting procedure and by normalising the spectrum at $0.55 \mu\text{m}$, yielding a formal 1-sigma error of $\pm 0.0127 \mu\text{m}^{-1}$. DeMeo et al. (2009) placed S-type spectra with slopes $> 0.25 \mu\text{m}^{-1}$ into a separate class, Sw. VF31 most likely lies outside the domain of this class, provided that the composite spectrum used here to compute the slope does not suffer from strong systematic effects.

It appears that an S-complex taxonomy is the most likely match to VF31. In the next Section we investigate further by searching among candidate “spectral analogue” objects and surfaces.

Table 3

Spectral comparison of VF31 with asteroids from the SMASS II and MITHNEOS surveys.

Asteroid					Asteroid				
No.	Name	Tax. Class	Geom. Albedo	$P_{\chi^2_{\mu}}$	No.	Name	Tax. Class	Geom. Albedo	$P_{\Phi_{\text{std}}}$
(4197)	Morpheus	Sq	0.370	21.8	(14)	Irene	S	0.159	17.6
(14)	Irene	S	0.159	18.0	(250)	Bettina	Xk	0.112	17.1
(250)	Bettina	Xk	0.112	14.1	(4197)	Morpheus	Sq	0.370	16.1
(57)	Mnemosyne	S	0.215	6.1	(887)	Alinda	S	0.310	7.6
(6)	Hebe	S	0.268	4.6	(57)	Mnemosyne	S	0.215	4.5
(887)	Alinda	S	0.310	4.6	(110)	Lydia	X	0.181	4.1
(925)	Alphonsina	S	0.248	3.3	(6)	Hebe	S	0.268	3.5

Table 4

Comparison of the VF31 spectrum with lunar spectra.

Data					Data				
ID	Feature	Type ^a	Quality ^b	$P_{\chi^2_{\mu}}$ (%)	ID	Feature	Type ^a	Quality ^b	$P_{\Phi_{\text{std}}}$ (%)
HA0813	HADLEY	MT	2	8.5	HA0813	HADLEY	MT	2	16.9
HA1082	LITTROW	MT	1	7.1	HB0908	CENSORINUS	CR(H)	3	10.6
HA0809	ARATUS	CR(H)	1	6.1	HA0819	APENNINE	MT	1	7.7
HB0804	LANGRENUS	CF(W)	1	6.1	H90426	DESCARTES	CR(H)	3	4.6
HB0908	CENSORINUS	CR(H)	3	5.9	HB0804	LANGRENUS	CF(W)	1	4.2
HA0819	APENNINE	MT	1	5.7	HA0847	BEER	CR(M)	3	3.3
HB0812	DESCARTES	CR(H)	2	5.4	HA1082	LITTROW	MT	1	3.0
HB0926	PLATO	CR(H)	4	4.7	HC1202	THEOPHILUS	CR(H)	4	3.0
HC1202	THEOPHILUS	CR(H)	4	4.6	HA0809	ARATUS	CR(H)	1	2.7
HE1186	FRA MAURO	CR(H)	4	3.0	HB0812	DESCARTES	CR(H)	2	2.4

^aCP: Central Peak, CR: Crater, CF: Crater Feature, H: Highlands, W: Wall, MT: Mountain, M: Mare;^bRanges from 1=Excellent to 5=Poor

3.2. Search for spectral analogues

3.2.1. Asteroids

Here we utilise asteroid spectra from the Small Main-Belt Asteroid Spectroscopic Survey, Phase II (SMASS II) and the MIT-UH-IRTF Joint Campaign for NEO Spectral Reconnaissance (MITHNEOS). We considered all asteroid spectra with both visible and near-infrared spectral coverage (427 in total) and applied the same P -ranking approach and cut-off criteria as in the previous Section. Top matches are listed in Table 3 and shown in the left panel of Figure 4 for the χ^2_{μ} statistic. The reported geometric albedo values are either from IRAS (Tedesco et al., 2004) or NEOWISE (Masiero et al., 2014). In addition, we have calculated principal components for these spectra and show them in Fig 3.

Individual asteroids that spectrally resemble VF31 belong to either the S- or X-complex, although none fit particularly well over the entire spectral region. Interestingly, P -ranking for the two scoring metrics highlights the same set of asteroids bar one, suggesting that the scoring is robust against the choice of statistical function.

In fact, the two scoring metrics identify the same top three asteroids: (4197) Morpheus (Sq), (14) Irene (S) and (250) Bettina (Xk). Of those, Bettina lacks the $2\mu\text{m}$ absorption while Morpheus fits the near-IR part rather well but shows a more pronounced $0.7\mu\text{m}$ peak than VF31. S-complex members are a better match to VF31's geometric albedo ($0.32^{+0.18}_{-0.11}$, Trilling et al., 2007) although the listed X-complex asteroids are within $2\text{-}\sigma$ of the measurement. Based on these considerations, we conclude that our best matches to VF31 are with S or Sq asteroids.

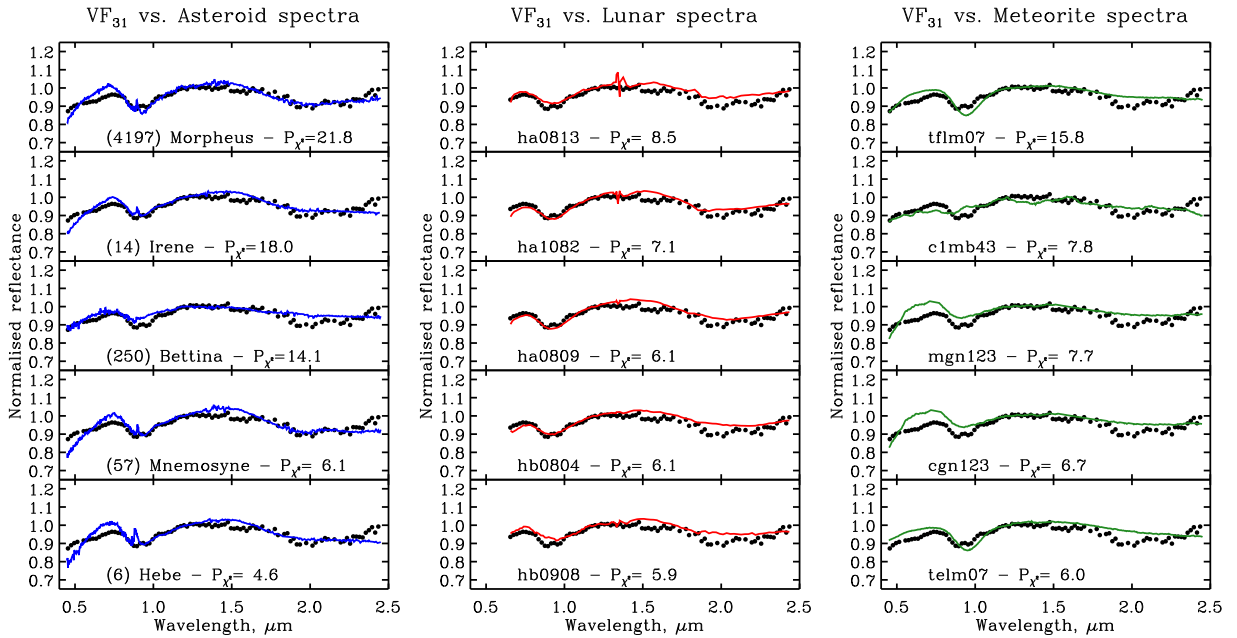
Rivkin et al. (2007) found that VF31 has a spectrum typical of pyroxene-dominated S-type asteroids classified as S(VII) in the Gaffey et al. (1993) sub-classification scheme. They compared its spectrum with those of two members of this subclass – (57) Mnemosyne and (40) Harmonia, both S-type asteroids. Mnemosyne is ranked 4th in our P_{χ^2} -sorted list and 5th in our $P_{\Phi_{\text{std}}}$ -sorted list. We compare the Mnemosyne and Harmonia spectra (green and red points resp.) with that of VF31 in Figure 5. Mnemosyne is overall the better match but does not fit well in the visible region.

<http://smass.mit.edu/catalog.php>

Table 5

Comparison of VF31 spectrum with RELAB meteorite spectra.

ID	Sample Name	Source	Type	$P_{\chi^2_{\mu}}$ (%)	ID	Sample Name	Source	Type	$P_{\Phi_{std}}$ (%)
tflm07	EETA79001,73	Mars	Shergottite	15.8	mgn153	Paragould	Other	LL5 Chondrite	12.1
c1mb43	Esquel	Other	Pallasite	7.8	mgn151	Paragould	Other	LL5 Chondrite	11.3
mgn123	Chainpur	Other	LL3 Chondrite	7.7	cgn151	Paragould	Other	LL5 Chondrite	11.3
cgn123	Chainpur	Other	LL3 Chondrite	6.7	mgn123	Chainpur	Other	LL3 Chondrite	10.8
telm07	EETA79001,73	Mars	Shergottite	6.0	cgn123	Chainpur	Other	LL3 Chondrite	6.4
mgp098	Murray	Other	CM2 Chondrite	5.5	cgn153	Paragould	Other	LL5 Chondrite	5.8
mgp086	Cold Bokkeveld	Other	CM2 Chondrite	5.4	tflm07	EETA79001,73	Mars	Shergottite	5.1
mgn151	Paragould	Other	LL5 Chondrite	5.3	cgp086	Cold Bokkeveld	Other	CM2 Chondrite	4.5
cgp098	Murray	Other	CM2 Chondrite	4.7	mgp086	Cold Bokkeveld	Other	CM2 Chondrite	4.4
cgn151	Paragould	Other	LL5 Chondrite	4.3	cgp098	Murray	Other	CM2 Chondrite	3.7
cbmb87	Y-74659	Other	Ureilite	3.6	mgp098	Murray	Other	CM2 Chondrite	3.7
mgn153	Paragould	Other	LL5 Chondrite	3.4	c1tb6	En95+CaS5	Other	Enstatite	3.5
cgp086	Cold Bokkeveld	Other	CM2 Chondrite	3.4	sblm03	Y-791197,90	Moon	–	2.7
cgn161	Rose City	Other	H5 Chondrite	3.2	telm07	EETA79001,73	Mars	Shergottite	2.4
mgn161	Rose City	Other	H5 Chondrite	3.1	cblm03	Y-791197,90	Moon	–	2.3
c1tb61	En95+CaS5	Other	Enstatite	3.1	mgn161	Rose City	Other	H5 Chondrite	2.1

**Figure 4:** Comparison of the VF31 spectrum (black dots) with spectra of different types of objects. Left: Asteroid spectra from SMASS II and MITHNEOS. Middle: Lunar surface spectra from PDS. Right: Meteorite spectra from RELAB.

3.2.2. The lunar surface

In our search for good spectral matches we also employed the Tool for Asteroid Modelling – M4AST to compare our combined spectrum with laboratory-measured spectra of various materials, lunar samples, meteorites and synthetic laboratory spectra in RELAB. In the process we found the best matches to be reflectance spectra of Apollo lunar

samples, motivating us to investigate this similarity in more detail. One problem in comparing VF31 with lunar samples is that those samples were disturbed when collected from the Moon and brought back to Earth. Therefore we used instead a set of ground-based reflectance spectra of the lunar surface available through the PDS Geoscience Node. The data consists of 359 spectra of small lunar areas (3–10 km across) covering the wavelength range 0.62–2.6 μm obtained at Mauna Kea Observatory (MKO) in Hawaii (McCord et al., 1981; Pieters, 1986). The top matches are listed in Table 4 and shown in Figure 4, middle panel. We observe the same high degree of commonality (8/10 entries) for our two scoring metrics as for the asteroid spectra. The visual similarity of the VF31 spectrum with the lunar surface spectra is remarkable. We obtain a good fit in the visible part for the feature around 0.75 μm , the 1 μm and 2 μm absorptions and the upturn in the flux beyond 2.1 μm . However, the 2 μm absorption is somewhat shallower in the lunar data.

3.2.3. Meteorites

Finally, we compared the VF31 spectrum with all available meteorite spectra in RELAB. The top hits are listed in Table 5 and presented in the right panel of Figure 4, where we used the same ranking procedure and cutoff criteria as for the asteroid and lunar spectra. There is again a high degree of commonality (75% or 12/16 entries) between the two scoring metrics. Overall, the 2 μm feature is either weakly present or altogether missing in the spectra and there is mismatch in the 1 μm absorption as well. We also note the presence of several Martian meteorites and of one lunar meteorite in the lists.

Our findings in Sections 3.2.1 - 3.2.3, taken together, suggest that lunar surface spectra are better matches to the VF31 spectrum than either asteroid or meteorite spectra. We test this further in the next Section.

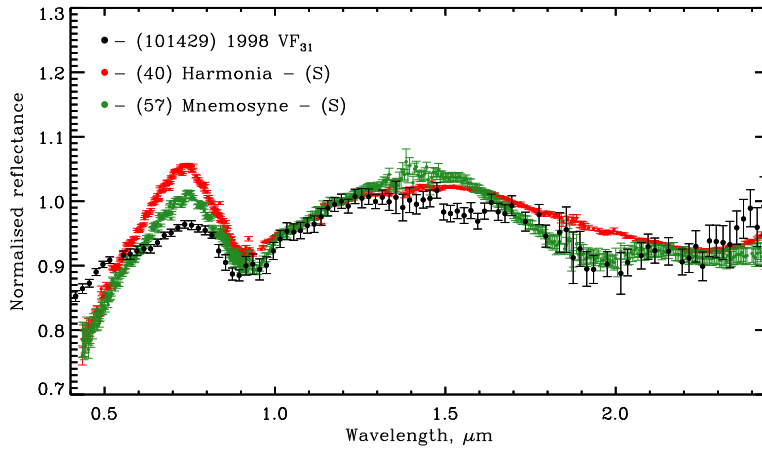


Figure 5: Comparison of our VF31 spectrum with the two asteroid analogues from Rivkin et al. (2007).

3.2.4. Ensemble ranking

Here we compare the VF31 spectrum with all types of available spectra simultaneously: asteroid, lunar surface or meteorite. To maintain consistency, we recompute $P_{\chi^2_\mu}$ and $P_{\Phi_{\text{std}}}$ values for a common wavelength range (0.656–2.455 μm) and resample to the same number of data points (93). We note that use of a common wavelength range will generally change the values of P from those presented in Tables 3, 4 and 5. In Table 6 we present P -ranking scores for the combined sample, showing all hits with $P_{\chi^2_\mu} > 3\%$ and the same number of elements for $P_{\Phi_{\text{std}}}$. The lists are dominated by lunar spectra (8 out of 10 listed matches) and complemented by some of the asteroid entries in Table 3, appearing in the bottom half of either list. All meteorite spectra score less than 3% for either statistic, therefore meteorite matches do not appear in these lists. The outcome of this exercise reinforces our earlier conclusion that lunar surface data are the best spectral match to VF31.

Table 6

Top-ranked members of the combined set of asteroid, meteorite and lunar surface spectra.

Name	Type ¹	Class	$P_{\chi^2_{\mu}}$ (%)	Name	Type ¹	Class	$P_{\Phi_{\text{std}}}$ (%)
HADLEY	LS	MT	7.4	HADLEY	LS	MT	15.3
LITTROW	LS	MT	5.9	CENSORINUS	LS	CR(H)	9.3
LANGRENUS	LS	CF(W)	5.2	APENNINE	LS	MT	6.8
CENSORINUS	LS	CR(H)	5.1	DESCARTES	LS	CR(H)	4.1
ARATUS	LS	CR(H)	5.1	LANGRENUS	LS	CF(W)	3.5
APENNINE	LS	MT	5.0	BEER	LS	CR(M)	2.8
DESCARTES	LS	CR(H)	4.3	(14) Irene	Ast	S	2.7
(4197) Morpheus	Ast	Sq	4.2	THEOPHILUS	LS	CR(H)	2.5
(14) Irene	Ast	S	4.2	LITTROW	LS	MT	2.5
PLATO	LS	CR(H)	3.8	ARATUS	LS	CR(H)	2.4
THEOPHILUS	LS	CR(H)	3.8	(250) Bettina	Ast	Xk	2.2

¹ Ast: Asteroid, Met: Meteorite, LS: Lunar surface

The top-ranked lunar surface spectra are from crater interiors and mountain features in the lunar highlands. Their composition is mainly anorthite ($\text{CaAl}_2\text{Si}_2\text{O}_8$) which is rare on the Earth as well as different kinds of magnesian (“mafic”) minerals, mainly pyroxene and olivine. Depending on the abundance of these minerals the $2\ \mu\text{m}$ absorption feature can be suppressed by different amounts (Clark et al., 2002). The weakness of the absorptions in the VF31 spectrum, with respect to other asteroids, may be due to the presence of agglutinates, which degrade diagnostic spectral absorptions, or the result of space weathering. The type of pyroxene present is probably responsible for the position of the $1\ \mu\text{m}$ feature. Low-Ca pyroxene (e.g. orthopyroxene - OPX) has an absorption at $0.93\text{--}0.95\ \mu\text{m}$ and high-Ca pyroxene (e.g. clinopyroxene - CPX) at $0.95\text{--}1.00\ \mu\text{m}$ (Zou et al., 2004). The presence of olivine broadens the former feature and suppresses the $2\ \mu\text{m}$ feature as well. The position of the $1\ \mu\text{m}$ feature observed in the spectrum of VF31 is consistent with OPX while the presence of the $2\ \mu\text{m}$ absorption indicates a moderate pyroxene abundance.

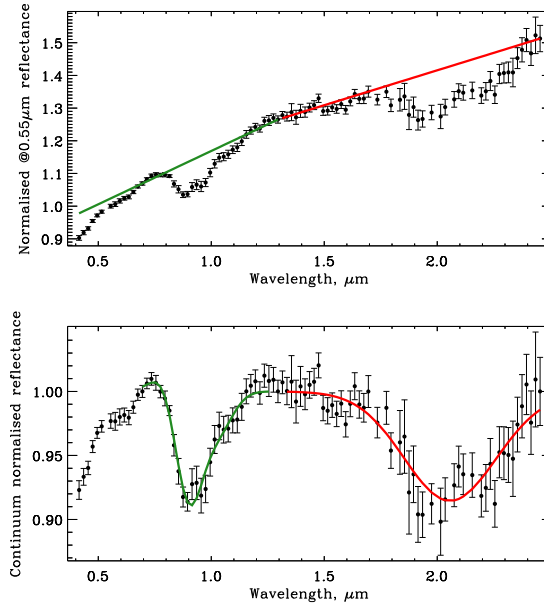


Figure 6: *Top:* Continuum fitting at the $1\ \mu\text{m}$ (green line) and $2\ \mu\text{m}$ (red line) absorptions. *Bottom:* Fits to the continuum-normalised spectrum around the 1 and $2\ \mu\text{m}$ features with Gauss-Hermite orthogonal functions (see text for details).

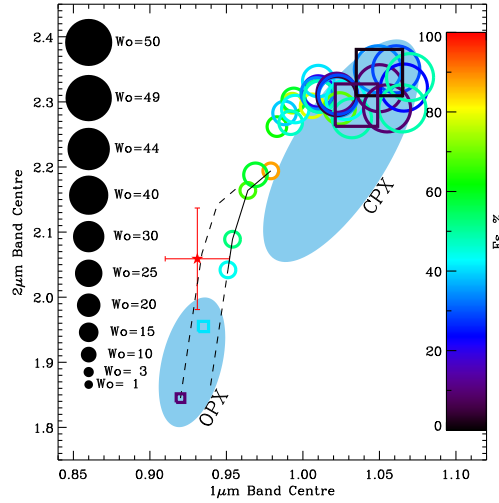


Figure 7: Position of 1 and 2 μm absorptions for VF31 (red star) and formal 3- σ uncertainties compared with RELAB data for pyroxene with different Wo and Fs numbers from Klima et al. (2011) and Horgan et al. (2014), represented by circles and squares respectively.

To obtain the positions of the absorption minima in our spectrum we follow the approach by Cappellari and Emsellem (2004) for identification of non-gaussian line profiles, using Gauss-Hermite series of orthogonal functions to fit the spectral lines. These are normalised gaussian functions multiplied by the linear combination of the 3rd and 4th order Hermite polynomials given by the following expressions:

$$G(y) = a \frac{1}{\sigma \sqrt{2\pi}} e^{-\frac{1}{2}y^2} \quad (3)$$

$$H_3(y) = h_3 \frac{1}{\sqrt{3}} (2y^3 - 3y) \quad (4)$$

$$H_4(y) = h_4 \frac{1}{\sqrt{24}} (4y^4 - 12y^2 + 3) \quad (5)$$

$$G_H = G(1 + H_3 + H_4) \quad (6)$$

where $y = (x - \mu) / \sigma$. The advantage of this approach is that it yields weakly-correlated parameter estimates (van der Marel and 1993). Here we perform a Levenberg-Marquardt nonlinear-least-squares fit (Moré, 1978) separately to the 1 and 2 μm features with the G_H function and obtain estimates for the set of coefficients $\{a, \mu, \sigma, h_3, h_4\}$ and formal 1- σ uncertainties. We are interested in the μ values, which represent the position of minimum absorption for the 1 and 2 μm features. In our case they are 0.931 ± 0.007 and $2.059 \pm 0.026 \mu\text{m}$ (Figure 6) respectively, which is more consistent with pyroxene low in Ca, e.g. OPX (Horgan et al., 2014).

We compare the positions of the 1 and 2 μm features with data in Klima et al. (2011) for which the Ca, Mg, Fe abundance is known. This sample is populated solely by CPX with Ca abundance (Wo number) $\geq 10\%$ and we complement this with data from Horgan et al. with low Wo number. The comparison is shown in Figure 7 where our measurement for VF31 is indicated by a red star. Data are represented as circles with different sizes to indicate Ca content and different colour to indicate Fe content. For measurements with low Ca content, i.e. Wo=10, there is sufficient data to indicate a trend with changing Fe abundance (solid line). If we extrapolate this trend to even lower Ca content (Wo=1; dashed line) we find that VF31 lies near this trend line, implying that its surface is highly abundant in OPX with moderate Fe abundance. Even if the uncertainty in the locations of the absorptions is underestimated by a factor of 3, VF31 is more consistent with OPX than CPX, especially in terms of the 1 μm feature (Figure 7).

There are several factors affecting the spectral profile of an asteroid surface: space weathering (Clark et al., 2002); regolith particle size, where smaller particles redden the slope and decrease the depth of absorption features (Reddy et al., 2015); a high content of iron or other mineral such as plagioclase; and phase reddening (PR; e.g. Sanchez et al., 2012).

Table 7

Results from mixture fitting of the VF31 spectrum. Entries in bold are also shown in Fig. 8.

Mineral or Mixture	Proportion %	SW wt% npFe	χ^2	Albedo
<i>Single minerals</i>				
OPX080	100	0.040	23.6614	0.20
OPX250	100	0.140	26.0996	0.14
OPX975	100	0.010	5.3495	0.50
OLVFo11	100	0.022	19.6011	0.23
OLVFo90	100	0.017	6.3926	0.48
Odessa Iron Meteorite	100	0	2.9552	0.13
Plagioclase (PGC)	100	0.009	2.7731	0.64
<i>Two-mineral mixtures</i>				
OPX080+Odessa	07/93	0	2.1076	0.13
OPX080+PGC	02/98	0.009	1.8963	0.59
OPX250+Odessa	05/95	0.005	2.1378	0.13
OPX250+PGC	01/99	0.011	1.8643	0.58
OPX975+Odessa	61/39	0.015	1.2762	0.24
OPX975+PGC	19/81	0.009	1.4207	0.59
<i>Three-mineral mixtures</i>				
OPX080+OLVFo90+Odessa	05/24/71	0.014	1.9456	0.17
OPX080+PGC+Odessa	06/56/38	0.018	1.2710	0.25
OPX170+OLVFo90+Odessa	05/27/68	0.018	1.9309	0.17
OPX170+PGC+Odessa	05/60/35	0.021	1.1878	0.25
OPX250+OLVFo90+Odessa	04/27/69	0.019	1.9102	0.17
OPX250+PGC+Odessa	04/58/38	0.020	1.2069	0.24
OPX500+OLVFo90+Odessa	11/27/62	0.021	1.7742	0.18
OPX500+PGC+Odessa	11/59/30	0.020	1.0407	0.27
OPX975+OLVFo90+Odessa	57/07/36	0.016	1.2532	0.25
OPX975+PGC+Odessa	46/30/24	0.016	1.1432	0.31
<i>Four-mineral mixtures</i>				
OPX080+OLVFo90+PGC+Odessa	06/00/56/38	0.018	1.2727	0.25
OPX250+OLVFo90+PGC+Odessa	04/00/57/39	0.023	1.2125	0.24
OPX975+OLVFo90+PGC+Odessa	44/04/30/22	0.016	1.1315	0.32

PR is relevant to VF31 because of the differing phase angles of the VIS and NIR observations for our composite spectrum (26° and 42° resp.; Table 1). However, PR strongly depends on taxonomic type, with olivine-rich asteroids being particularly susceptible to it (Perna et al., 2018). Because we do not see evidence of PR on spectra of the olivine-dominated Eureka family observed at 2°-27° phase angle (see Section 4), we believe our spectrum of VF31 is not significantly affected either.

With the information gathered so far, we can perform mixture fitting to the VF31 spectrum. In particular, we use the spectral slope to constrain the combination of space weathering, iron content and/or particle size that best matches the spectrum. Our analysis so far strongly indicated the presence of OPX; we adopt this mineral as one of the baseline endmembers in this exercise.

3.2.5. Mixture fitting

We model the spectrum of VF31 using candidate mineral components in a simplified Hapke spectral mixing model (Hapke, 1981, 1984, 1986). In the case of intimately mixed material, such as asteroid regolith, the observed spectrum does not correspond to the linear combination of the individual component spectra. However, using the Hapke reflectance theory one can convert the reflectance spectrum (r) of individual components to their single scattering albedo (w) which, under Hapke theory, can be linearly combined. The linear combination of single scattering albedo can then be transformed back to the reflectance spectrum and compared to the asteroid spectrum.

We combine spectra of several candidate end-members to find satisfactory fits to the asteroid spectrum. From the fitting procedure, we obtain the relative abundance of each end-member. Unlike the P -ranking described in previous

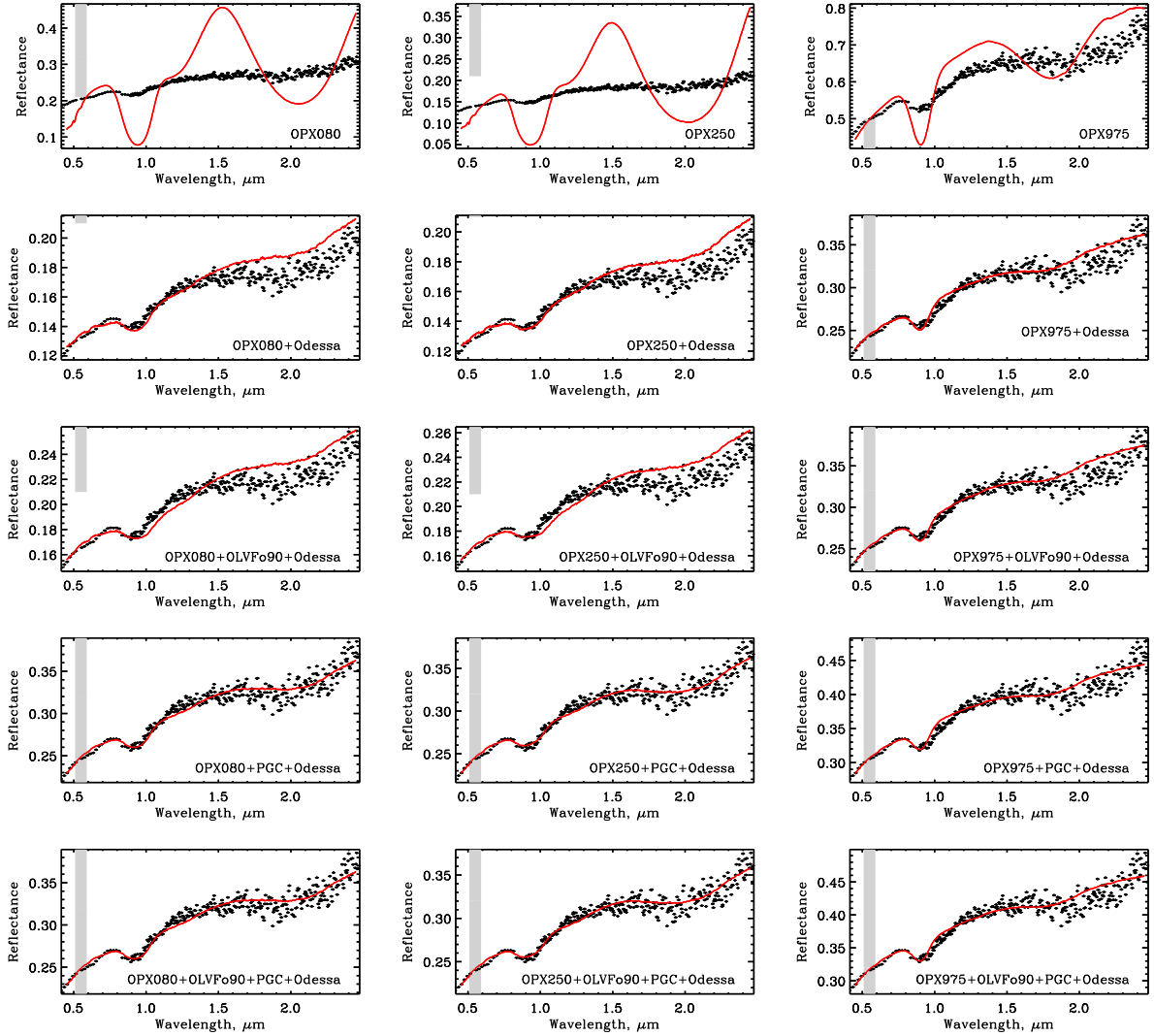


Figure 8: Selected mixture models for VF31 from Table 7. The number of elements increases from top to bottom. The grey vertical band indicates the 1- σ range in the albedo.

Sections, here we use the unbinned spectral data for VF31 in the fits. In addition, we account for space weathering using the Hapke (2001) procedure by adding npFe nanophase iron within the host material while taking into account the optical constants of iron. Details on the mixing and space-weathering procedures applied to asteroids can be found in Devogèle et al. (2018).

Selected fits from our mineralogical analysis are listed in Table 7 with items in bold also shown in Fig 8. First, we compared the observed spectrum of VF31 with individual end-member spectra from RELAB. These included: orthopyroxene (OPX), olivine (OLV), plagioclase (PGC) and the iron meteorite MET101A (Odesa). We find that Mg-rich mineral endmembers (OPX97.5, OLVfo90) are better matches than iron-rich endmembers (OPX08, OLVfo11) though the fits are generally unsatisfactory and with too high albedos. The best single-endmember fits were achieved by either iron meteorite or plagioclase, however the high albedo of the latter and low albedo of the former are inconsistent with the VF31 measurement.

Next, we consider mixtures of two or more elements. Here it is important to note that, for groups with a fixed number of elements, the $\Delta\chi^2$ value at even a 1- σ level of significance is >2 . Therefore, the information on Table 7 should be viewed as groups of potential matches, similar to the P -ranking approach used earlier in the paper, where all

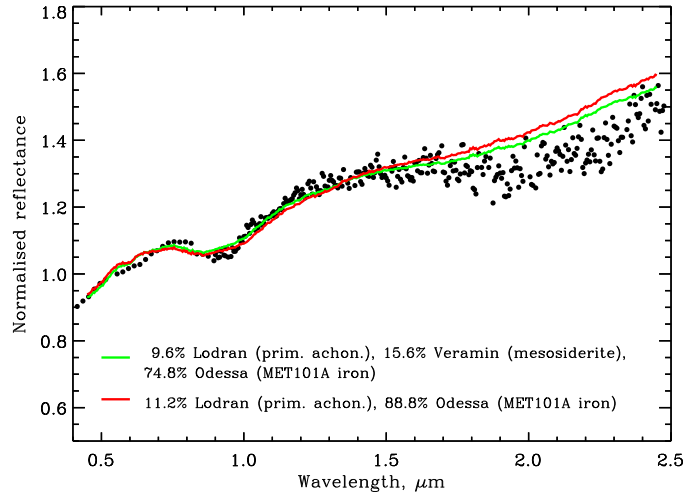


Figure 9: Mixture fitting with achondrite meteorite endmembers from Rivkin et al. (2007) and including the Odessa iron meteorite.

mixtures in the same group are statistically equivalent. The best-fit mixtures among the different groups are determined by visual inspection, taking into account the asteroid albedo and the number of elements in the mixture.

Our best-fit two-element mixture is OPX with high (97.5%) Mg content combined with iron meteorite in proportions of 61% and 39% respectively (right panel, second from top in Figure 8). This mixture is also consistent with the albedo at the $1\text{-}\sigma$ level. As a simple robustness test of the fit, we replaced the Odessa spectrum with the average for all available iron meteorite spectra in RELAB. This does not noticeably alter the result and we retained use of the Odessa spectrum for the remainder of the exercise. Reducing the Mg content in OPX results in the fits shown in the left and middle panels. These are better matches to the shape and location of the $2\text{ }\mu\text{m}$ absorption though they also show a higher slope in that region. However, they are inconsistent with the asteroid albedo and we find this to be true also if we replace the iron meteorite with other endmembers.

If we allow a third element in the mixture, we find that olivine has little effect on the spectral profile but adding plagioclase results in visually satisfactory fits for mixtures with low-to-moderate OPX that are also consistent with the albedo. Interestingly, these mixtures are dominated by the PGC and iron metal components (94-96%) rather than OPX (4-6%). In contrast, Mg-rich OPX accounts for 50% or more in the respective three-element mixture. The presence of plagioclase would actually be consistent with the spectral similarity of VF31 to the lunar surface (Section 3.2.2). Plagioclase was also identified as one of the main surface constituents of asteroid Itokawa through examination of material returned to Earth by the Hayabusa spacecraft (Yoshikawa et al., 2015). The effect of OPX composition on absorption band location for the three-element mixtures can be better illustrated by plotting one band against the other. We have calculated the 1 and $2\text{ }\mu\text{m}$ band locations for the different mixtures in the same way as we did for VF31 in the previous Section and plotted them in Figure 10. The error bars for VF31 are $3\times$ the formal uncertainty. Clearly, three-element mixtures that include OPX at 8-50 % Mg abundance and plagioclase are more compatible with VF31 than mixtures with either olivine or Mg-rich OPX.

Allowing both PGC and olivine in a four-element mixture and re-optimising (bottom row) has the effect of pushing the olivine out of the mixture and we recover the OPX-PGC-Odessa solution, in other words there is no further improvement in fit quality. All mixtures shown in Figure 8 yield similar abundances of npFe, 1.4-2.3% by weight, with the exception of the two-element low-to-moderate OPX mixtures (0-0.5% by weight).

For completeness, we have also fit the spectrum to two mixtures with meteorite material presented in Rivkin et al. (2007) – Lodran (primitive achondrite), Veramin (mesosiderite) and Odessa (iron) (Figure 9). In those cases, the spectral profile shortward of the $1\text{ }\mu\text{m}$ absorption in the meteorite mixture is shifted to shorter wavelengths and the $2\text{ }\mu\text{m}$ feature becomes quite shallow. The fits are somewhat similar to the two-element low-OPX mixtures in Fig. 8. The χ^2 values obtained here are 1.68 and 2.03 for the 3- and 2- member mixtures respectively and with albedos of

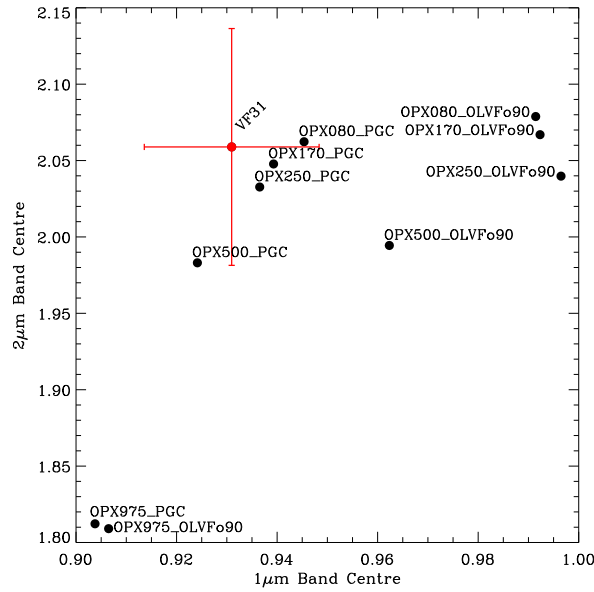


Figure 10: Positions of 1 and 2 μm absorptions of OPX three-element mixtures containing olivine, plagioclase, and meteoritic iron compared to VF31.

0.13 and 0.12 which are rather low for VF31.

In conclusion, the simplest mixture which adequately represents the spectrum of VF31 is Mg-rich orthopyroxene mixed with iron. The most promising alternative appears to be a mixture of iron and plagioclase with a small amount of Mg-poor orthopyroxene. This mixture better reproduces the shape and location of the 2 μm absorption at the expense of introducing an extra degree of freedom to the model. Though based on the best information available at this time, our mixture fitting results should be treated with some caution as they depend on combining measurements from different spectral regions obtained under different sets of circumstances. For this reason, we have strived to describe our data reduction and analysis in detail so that its advantages or shortcomings are clear to the reader.

4. Eureka family asteroids

Eureka family asteroids (311999) 2007 NS₂ and (385250) 2001 DH₄₇, referred to as NS2 and DH47 hereafter, were observed with X-SHOOTER (Table 1). Their spectra, together with a (5261) Eureka spectrum obtained in 2005 as part of the the MIT-Hawaii Near-Earth Object Spectroscopic Survey (MITHNEOS) are presented in Figure 11. All spectra have been normalised to 0.55 μm .

The spectra of NS2 and DH47 virtually coincide in the range 0.52-0.78 μm and diverge from $\sim 0.8 \mu\text{m}$ onwards. This can be more clearly seen by plotting the spectral ratio (Figure 12, top panel). Eureka's spectrum is indistinguishable, within uncertainties, from the other two up to 0.7 μm (bottom panel) but shows a higher relative reflectance than either asteroid longward of that wavelength.

There is a drop in the reflectance of NS2 relative to DH47 between 1 and 1.05 μm . A similar feature, although less pronounced, may be present in the spectrum of DH47 as well. The slope behaviour of the two spectra is very similar between 1 and 1.7 μm . Over the same range the relative reflectance of NS2 is lower than that of DH47.

Although space weathering may be causing some of the differences in the spectra, it is probably not solely responsible for them. Laboratory experiments show that space weathering in olivine (in the form of npFe formed by heating) changes the slope over the entire spectrum, not preferentially the red or blue part (eg Kohout et al. (2014), their Figure 6, bottom panel; also Kaluna et al. (2017)). Production of npFe by heating (Kohout et al.), laser irradiation (Yamada et al., 1999; Sasaki et al., 2001b), irradiation by H⁺, He⁺, Ar⁺, and Ar₂ (Brunetto and Strazzulla, 2005) change spectra in different ways but all show reddening (see also Figure 1 in Sasaki et al. (2001a)). Olivine appears to be more easily weathered than pyroxene (Yamada et al., 1999; Hiroi and Sasaki, 2001).

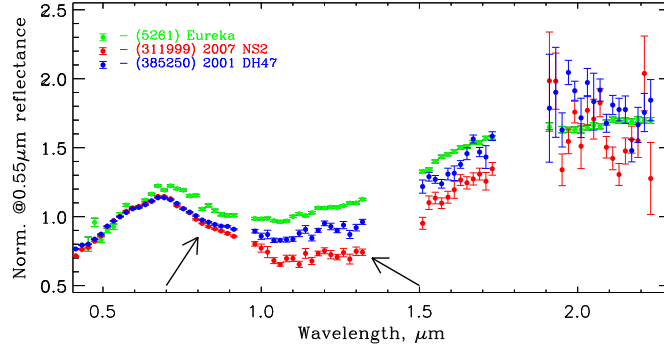


Figure 11: Reflectance spectra of (5261) Eureka, (311999) 2007 NS₂ and (385250) 2001 DH₄₇. The “shoulders” referred to in the text are marked with arrows.

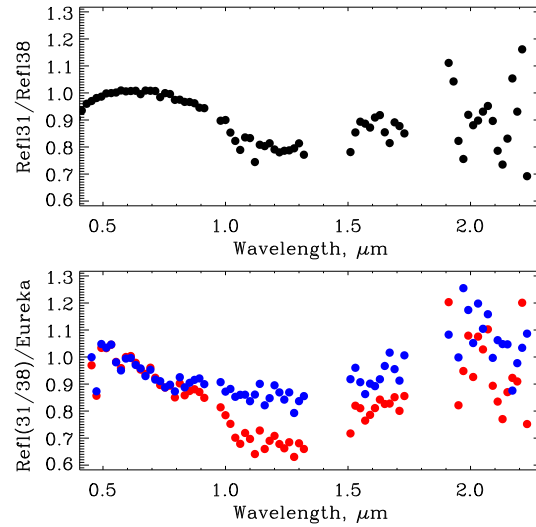


Figure 12: Comparison of spectra of Eureka family members. *Top:* NS2 divided by DH47. Note the coincidence in the spectral profiles up to $\sim 0.8 \mu\text{m}$. *Bottom:* NS2 (red) and DH47 (blue) divided by Eureka.

If the differences in the two spectra are not solely due to space weathering, they can be due to any combination of space weathering with: (a) phase reddening (b) different particle size distribution, or (c) composition. We discuss each process separately below.

Phase reddening: Phase reddening increases the spectral slope and decreases the strength of the absorption features with increasing phase angle. Sanchez et al. (2012) found differences in the spectral slope of NEAs observed at different phase angles. The same authors obtained laboratory spectra of olivine-rich LL6 chondrite material at different phase angles and found significant differences in the near-IR for phase angles $>30^\circ$ (cf their Figures 5 and 6; see also Perna et al., 2018). Our observations were obtained at phase angles $<30^\circ$ (Table 1) therefore our spectra should not be strongly affected by phase reddening. Indeed, we expect the spectral slope should increase with the phase angle, but here the opposite is true, i.e. the spectral slope for Eureka is $0.3329 \pm 0.0008 \mu\text{m}^{-1}$ (phase angle $\sim 4.5^\circ$), $0.1818 \pm 0.0032 \mu\text{m}^{-1}$ for DH47 (phase angle $\sim 13^\circ$) and $0.1439 \pm 0.0037 \mu\text{m}^{-1}$ for NS2 (phase angle $\sim 26^\circ$).

Surface particle size: Cloutis et al. (2015) show that the $1 \mu\text{m}$ absorption in samples of particulate olivine broadens and the spectrum darkens as the grain size increases from $45 \mu\text{m}$ to $500\text{--}1000 \mu\text{m}$ (left panel of Figure 13). Also, “shoulder” features (marked with arrows) at ~ 0.8 and $\sim 1.3 \mu\text{m}$ are symmetric around the main absorption at $\sim 1 \mu\text{m}$

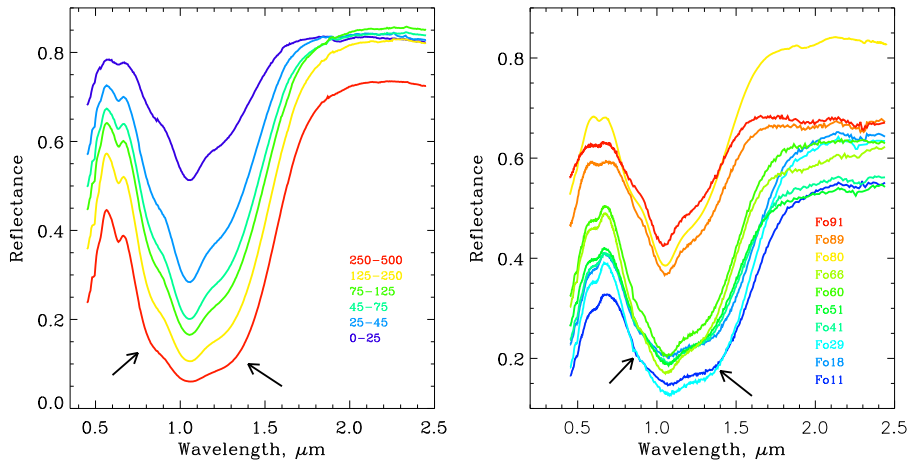


Figure 13: *Left:* Spectra of particulate olivine with different particle size. *Right:* Spectrum of olivine with different Fo number. The shoulders referred to in the text are marked with arrows.

and flatten when decreasing the grain size. These shoulders are due to the overlapping α , β and γ bands of olivine with γ being 3-5 times stronger than α and β (Burns, 1970). NS2 has a deeper absorption and a more prominent shoulder at $\sim 1.3 \mu\text{m}$. So a smaller surface grain size on the surface of DH7 than in NS2 could explain the differences in the two spectra. The shallower $1 \mu\text{m}$ absorption feature for Eureka could indicate the presence of yet smaller grains on its surface than the other two asteroids.

Composition: Changing the Fe to Mg ratio or Fo number of olivine affects the width of the $1 \mu\text{m}$ feature as well as the reflectance. Smaller Fo numbers, i.e. higher content of Fe, have a wider $1 \mu\text{m}$ feature and lower albedo (right panel of Figure 13). The effect on the spectral profile is similar to that for particle size. In particular, the shoulders flatten when the Fo number increases. In our spectra they are non-symmetric around $1 \mu\text{m}$ with the one from the longward side of the absorption being more prominent than from the shortward one. An alternative explanation for the differences in the spectra of the observed asteroids could therefore be that the olivine on the surface of NS2 is more Fe-rich than for DH47 and that Eureka has more Mg-rich olivine than the other asteroids.

We conclude that the differences in the spectra between the Eureka family asteroids, if not due to systematics introduced during data acquisition and/or reduction, are caused by space weathering in combination with differences in surface particle size and/or a different composition in terms of olivine Fo number. Because the shoulder from the longward side of the $1 \mu\text{m}$ feature is more prominent in the spectra than the shoulder below $1 \mu\text{m}$, the dominant effect should be the difference in olivine composition, with NS2 more Mg-rich than DH47 and Eureka, and Eureka itself being more Fe-rich than the others.

5. Conclusions and origin implications

Eureka family asteroids share a common olivine-dominated composition (Borisov et al., 2017), yet our analysis shows measurable differences between their spectra. We found these to be attributable to more than one causes: space weathering, particle grain size or composition. This last possibility would imply differences in the type of olivine between the three asteroids.

VF31 is the only L5 Trojan asteroid not part of the Eureka family. Its mineralogy is quite different from its companions; our analysis shows that it is spectrally similar to areas in the lunar highlands. The simplest spectral mixture that adequately represents VF31 features Mg-rich orthopyroxene and metallic iron as its principal ingredients. This interpretation is not unique and a better visual fit is achieved with mixtures dominated by iron metal and plagioclase with a small contribution by Mg-poor orthopyroxene.

Our study is based in part on observations by Rivkin et al. (2007), therefore it is not surprising that this study's conclusions overlap with that work. Those authors placed VF31 within the pyroxene-rich S(VII) subclass of the

Gaffey et al. (1993) classification scheme for S-type asteroids, a finding that led them to compare the asteroid spectrum with mixtures of iron-rich meteorite and primitive achondrite endmembers. Here we confirm the prevalence of iron metal and the existence of pyroxene. Identification of the latter is facilitated by the higher S/N of our visible spectrum while the former does a better job than our space weathering model at weakening the pyroxene absorption to match the observations. Additionally, we find that the best fits to the data are mixtures of orthopyroxene and meteoritic iron with or without plagioclase, rather than iron-rich primitive achondrites (Rivkin et al., 2007). The two interpretations are not mutually exclusive; the difference between Rivkin et al. and this work is probably due to the increased availability of laboratory-measured endmember spectra for fitting since the previous study, rather than a fundamental difference between their approach and ours. Rapid progress in modelling the solar system's formation and early evolution also allows for a broader discussion on this asteroid's origin than was possible ten years ago. Below we examine the different types of candidate parent bodies and discuss the implications on a case-by-case basis, beginning with the proposed association with primitive achondrites, specifically the Acapulcoite-Lodranite (AL) meteorite group linked to S-type asteroids (McCoy et al., 2000).

The provenance of AL meteorites was recently investigated by Neumann et al. (2018) using thermo-chronological modelling of potential parent bodies. They found the best-fit source objects to be large (200–400 km), partially differentiated planetesimals that formed relatively close to the Sun a few Myr after Calcium Aluminium-rich Inclusions, probably earlier and at a smaller heliocentric distance than the parent bodies of ordinary chondrites. These may still exist among the few tens of >200 km Main Belt asteroids, a possibility also supported by the inferred shallow (~ 10 km) excavation depth. Alternatively, they may have been shattered and collisionally dispersed during the early evolution of the terrestrial planets.

If the presence of iron on the surface of VF31 does not reflect the original mineralogy of the parent body, it could represent extreme space weathering due to the asteroid's long residence time at 1.5 AU from the Sun. Solar radiation intensity on the Martian Trojans is higher than for any Main Belt asteroid. Mars Crossers (MCs) and Near Earth Asteroids (NEAs), which come closer to the Sun, have typical dynamical lifetimes of $\lesssim 10^8$ yr before being lost to collisions or dynamical ejection (Bottke et al., 1994), $\sim 40\times$ less than the Trojans if the latter are primordial. Indeed, an NEA on a near-circular orbit resembling that of the Trojans would need to be located at $a \lesssim 1.5/\sqrt{40} \simeq 0.23$ AU from the Sun to accumulate the same amount of incident solar energy over a period of 10^8 yr.

Our analysis shows a remarkable similarity between VF31 and the lunar surface. A quantitative assessment of the likelihood that VF31 could have originated from the Moon is beyond the scope of this work, yet it is reasonable to ask if this is at least possible. To answer this, we break the problem into the following sub-problems: i) Ejection from the Moon ii) Transfer from the orbit of the Earth to an VF31-like orbit, and iii) Insertion into Mars's Trojan clouds.

An impact ejectum with a velocity higher than the Moon's escape velocity of 2.4 km/s will leave its gravity field. To place this body in a heliocentric orbit, the ejection velocity should also exceed 3.5 km/s (Gladman et al., 1996). According to Melosh (1984), a 1-km diameter object with this ejection velocity is produced by an impact with a projectile of incident speed of 10 km/s and radius 125 km to produce a 974 km diameter crater (Asphaug, 1997). This is considerably smaller than the size of the largest lunar basin (Neumann et al., 2015, D=2400 km), therefore this scenario is at least plausible.

Once the object is in heliocentric orbit, it must somehow find itself at an orbit similar to that of VF31, namely with a semi-major axis $a=1.52$ AU and an inclination $i=31.5^\circ$. Here we consult the simulations by Gladman et al. (1995) who investigated the dynamical evolution of lunar impact ejecta. From their Figure 9, it indeed appears possible to reach such an orbit following escape from the Earth-Moon system.

The phase that relates to the last sub-question is potentially the most challenging as the object needs to be captured in stable libration around one of the Lagrange points of Mars. This scenario is virtually impossible in the present era (Polishook et al., 2017) but plausible during the final stages of terrestrial planet formation, when the orbit of Mars may have been perturbed by lunar-sized objects, resulting in a chaotic wandering of its semi-major axis (Scholl et al., 2005). In that case, the observed Martian Trojan asteroids were captured during one of the last semi-major axis jumps. A km-size fragment of the Moon could have been produced, for instance, during the Late Heavy Bombardment (LHB) 3.9 ± 0.1 Ga ago (Tera et al., 1974; Hartmann et al., 2000) yet, if Mars formed 4.5 Ga ago and its orbit stabilised in less than 200 Myr (Polishook et al., 2017), a link between VF31 and the LHB appears unlikely. If we accept a lunar origin for the asteroid we must therefore conclude that it was ejected earlier, perhaps as soon as the lunar crust solidified (eg Marks et al., 2019), or produced during the original cataclysmic event thought to have created our natural satellite (Hartmann and Davis, 1975).

Alternatively, this asteroid may have originated from Mars itself. Polishook et al. (2017) recently proposed that

the olivine-rich Mars Trojans at L5 originate from the martian mantle, having been excavated by an impact similar to that responsible for the hemisphere-wide Borealis basin (Andrews-Hanna et al., 2008). Initially deposited near the Martian orbit, the asteroids were captured permanently at L5 as Mars “jumped” to its present orbit in the final stages of its formation (Scholl et al., 2005). Although VF31 has higher orbital inclination than the olivine-rich Trojans, the dynamical component of this scenario will probably also work for that asteroid. However, the pyroxene-rich composition of (101429) is more compatible with crustal, rather than mantle, material (Zuber, 2001). In this context, our finding of strong iron metal contribution to the spectrum, if not related to space weathering, may be linked to the generally high abundance of iron oxides on the Martian surface (Bibring et al., 2005).

The Martian origin scenario is broadly consistent with our present understanding of Mars’s surface and shallow interior composition, as a Borealis-scale impact would likely have ejected fragments of both crust and mantle into space. Pyroxene abundance on Mars’s surface follows the planet’s hemispherical dichotomy (Bibring et al., 2005; Mustard et al., 2005; Riu et al., 2019). Orthopyroxene (Low Calcium Pyroxene; LCP) is generally less abundant than clinopyroxene (High Calcium Pyroxene; HCP) and enriched in the older Noachian-era crust, while HCP is enriched in more recent lava flows, implying that the crust likely formed out of a fully melted magma where LCP and HCP were well mixed (Bibring et al., 2009). Our interpretation of the type of pyroxene present on the asteroid is somewhat at odds with the relative abundances of martian LCP and HCP; it could indicate depth-dependent survival of ejecta as intact chunks of material, with near-surface LCP-rich deposits more likely to survive than HCP-rich material deeper down; or simply a prevalence of LCP at the source depth on the time of ejection. The latter interpretation would be consistent with formation models of Noachian-era terrain (Mustard et al., 2005) and suggests that the asteroid originated as a piece of Mars’s ancient crust, dating from the earliest period of its existence.

Finally, we must also consider the possibility that VF31 is not a primordial occupant of the L5 cloud of Mars but was captured later, after the architecture of the solar system has settled into its observed configuration. Christou et al. (2020) raised this possibility in relation to the close proximity of VF31’s orbit to a secular resonance; their numerical simulations suggested that the Yarkovsky effect may have helped to stabilise the orbit post-capture. If that is the case, the most likely parent bodies of VF31 would then be extant or extinct S-type asteroids in the Main Belt (MB), probably its inner part. Dynamical transport from the MB to the Mars-crossing population tends to preserve the orbital inclination, therefore we favour a high-inclination source such as the Hungaria or Phocaea families (Migliorini et al., 1998). For instance, asteroids in the pyroxene-dominated Gaffey S(VII) subclass exist in the region occupied by the Hungarias, though with generally low abundance (Lucas et al., 2017).

6. Prospects for Future Investigation

We consider the present analysis of the L5 Martian Trojan asteroids and especially VF31 as the most detailed investigation of their mineralogy to-date. At the same time, we are aware of alternative approaches to mineralogical analysis of asteroid spectra, for instance through the Modified Gaussian Model (MGM; Sunshine and Pieters, 1998; Sunshine et al., 2004) and we encourage their application on these data to obtain additional insight into these fascinating objects. Inevitably, however, making further progress in studying the Trojans will require the acquisition of new data.

The Large Synoptic Survey Telescope (LSST) should begin operations in 2022 and will eventually generate the largest catalog of Solar System objects to date - as faint as $r=25$ - as well as obtain *ugrizy* colours (Ivezić et al., 2019). It should find a few hundred additional members of the Eureka family (Christou et al., 2020) and constrain the taxonomy of many of these new discoveries. Colours may be used to diagnose spectral differences among family members. From Figure 11 we expect, for example, similar reflectance around $0.6\ \mu\text{m}$ but significant differences at $1.0\ \mu\text{m}$, the central wavelengths of the *r* and *y* filters respectively. The projected 10 years of LSST nominal survey operation will span 5 different oppositions of the Mars Trojans, allowing also to characterise the spectral dependence on phase angle.

Higher quality visible and near-IR spectra on these faint asteroids could be obtained by the spectrograph (Rodrigues et al., 2018) on the planned European Extremely Large Telescope (E-ELT; Gilmozzi and Spyromilio, 2008). Observations on yet longer wavelengths diagnostic of olivine composition have been previously obtained only for Eureka by the *Spitzer* space telescope (Lim et al., 2011). The soon-to-be-launched James Webb Space Telescope (JWST) will bring much improved spectrophotometric capabilities to asteroid studies in this part of the electromagnetic spectrum (Rivkin et al., 2016). Indeed, the superior sensitivity and spectral coverage of JWST allows the acquisition of high quality visible, near-IR and mid-IR spectra for much of the Eureka family as well as for (101429). This will allow more spectral comparisons of the type attempted here and over a wider spectral region.

Yet more comprehensive studies of these objects will likely require a spacecraft visit which could, en route to the

Trojans, obtain spectra at Mars or the Moon for direct comparison with the asteroid data (Wickhusen et al., 2017).

7. Acknowledgments

We thank the two reviewers, David Polishook and Tomas Kohout, for their insightful comments that led to a considerably improved manuscript. This work was supported via grants (ST/M000834/1 and ST/R000573/1) from the UK Science and Technology Facilities Council. Astronomical research at the Armagh Observatory and Planetarium is grant-aided by the Northern Ireland Department for Communities.

Based on observations collected at the European Organisation for Astronomical Research in the Southern Hemisphere under ESO programme 296.C-5030 (PI: A. Christou).

This research utilises spectra acquired with the NASA RELAB facility at Brown University.

Eureka spectral data utilised in this publication were obtained and made available by the MIT-UH-IRTF Joint Campaign for NEO Reconnaissance. The IRTF is operated by the University of Hawaii under Cooperative Agreement no. NCC 5-538 with the National Aeronautics and Space Administration, Office of Space Science, Planetary Astronomy Program. The MIT component of this work is supported by NASA grant 09-NEOO009-0001, and by the National Science Foundation under Grants Nos. 0506716 and 0907766.

This publication makes use of data products from the Near-Earth Object Wide-field Infrared Survey Explorer (NEOWISE), which is a project of the Jet Propulsion Laboratory/California Institute of Technology. NEOWISE is funded by the National Aeronautics and Space Administration.

We thank Andrew Rivkin for providing us with the SpeX NIR spectrum of (101429) 1998 VF31 and Boris Nedelchev for his suggestion to use Gauss-Hermite series polynomials in fitting the absorption features in the VF31 spectrum and discussions on the statistical significance of our mixture fits.

A. Ranking of spectral matches

In our spectral matching procedure (Section 2.2), we assume the following simple error model:

- given a spectral measurement x_i and its error σ_i , the real value X_i is described by a Gaussian distribution with mean x_i and standard deviation σ_i (we assume uncorrelated measurement errors).
- the distribution of the possible observed values is a Gaussian with mean X_i and standard deviation σ_i , assuming that our experimental σ_i are good estimates of the real error.

Note that the two assumptions above are equivalent to assuming that the distribution of the possible observed values is a Gaussian with mean x_i and standard deviation $\sqrt{2}\sigma_i$, however the factor $\sqrt{2}$ has a small effect in the computations.

The cost functions χ_μ^2 and Φ_{std} cannot be reduced to a standard χ^2 statistic. Therefore, we cannot take advantage of the known properties of the χ^2 distribution and instead follow a numerical approach:

- we generate a large number of clones of the observed spectrum substituting each measurement x_i with a random quantity x'_i generated from a parent Gaussian distribution with mean x_i and standard deviation $\sqrt{2}\sigma_i$
- each clone of the observed spectrum is normalised at the common normalisation wavelength
- for each clone of the observed spectrum the cost functions are computed using x'_i instead of x_i , a new ranking list is built, and the top-ranked model identified.

This approach allows to count the number of times a given model spectrum is ranked at the top of the score list and estimate the corresponding probability P of being the top-ranked model.

References

- J. C. Andrews-Hanna, M. T. Zuber and W. B. Banerdt, 2008. The Borealis basin and the origin of the martian crustal dichotomy. *Nature* 453, 1212–1215. doi:10.1038/nature07011.
- E. Asphaug, 1997. Impact origin of the Vesta family. *Meteoritics and Planetary Science* 32, 965–980. doi:10.1111/j.1945-5100.1997.tb01584.x.

- J.-P. Bibring et al., 2009. OMEGA: observatoire pour la minéralogie, l'eau, les glaces et l'activité, in: A. Chicarro, O. Witasse and A. P. Rossi (Eds.), *Mars Express: Summary of Scientific Results*, pp. 75–96.
- J.-P. Bibring et al., 2005. Mars surface diversity as revealed by the OMEGA/Mars Express observations. *Science* 307, 1576–1581. doi:10.1126/science.1108806.
- G. Borisov, A. Christou, S. Bagnulo, A. Cellino, T. Kwiatkowski and A. Dell'Oro, 2017. The olivine-dominated composition of the Eureka family of Mars Trojan asteroids. *MNRAS* 466, 489–495. doi:10.1093/mnras/stw3075, arXiv:1701.07725.
- J. Bottke, W. F., M. C. Nolan, R. Greenberg and R. A. Kolvoord, 1994. Collisional lifetimes and impact statistics of Near-Earth Asteroids, in: *Hazards Due to Comets and Asteroids*, p. 337.
- R. Brunetto and G. Strazzulla, 2005. Elastic collisions in ion irradiation experiments: A mechanism for space weathering of silicates. *Icarus* 179, 265–273. doi:10.1016/j.icarus.2005.07.001.
- R. G. Burns, 1970. Crystal field spectra and evidence of cation ordering in olivine minerals¹. *American Mineralogist* 55, 1608–1632. arXiv:https://pubs.geoscienceworld.org/ammin/article-pdf/55/9-10/1608/4250103/am-1970-1608.pdf.
- M. Cappellari and E. Emsellem, 2004. Parametric recovery of line-of-sight velocity distributions from absorption-line spectra of galaxies via penalized likelihood. *PASP* 116, 138–147. doi:10.1086/381875, arXiv:astro-ph/0312201.
- A. A. Christou, 2013. Orbital clustering of martian Trojans: An asteroid family in the inner Solar System? *Icarus* 224, 144–153. doi:10.1016/j.icarus.2013.02.013, arXiv:1303.0420.
- A. A. Christou, G. Borisov, A. Dell'Oro, S. A. Jacobson, A. Cellino and E. Unda-Sanzana, 2020. Population control of Mars Trojans by the Yarkovsky & YORP effects. *Icarus* 335, 113370. doi:10.1016/j.icarus.2019.07.004, arXiv:1907.12858.
- B. E. Clark, B. Hapke, C. Pieters and D. Britt, 2002. Asteroid space weathering and regolith evolution. pp. 585–599.
- E. A. Cloutis et al., 2015. Olivine-metal mixtures: Spectral reflectance properties and application to asteroid reflectance spectra. *Icarus* 252, 39–82. doi:10.1016/j.icarus.2014.10.003.
- F. E. DeMeo, R. P. Binzel, S. M. Slivan and S. J. Bus, 2009. An extension of the Bus asteroid taxonomy into the near-infrared. *Icarus* 202, 160–180. doi:10.1016/j.icarus.2009.02.005.
- F. E. DeMeo et al., 2019. Olivine-dominated A-type asteroids in the main belt: Distribution, abundance and relation to families. *Icarus* 322, 13–30. doi:10.1016/j.icarus.2018.12.016.
- M. Devogèle et al., 2018. New polarimetric and spectroscopic evidence of anomalous enrichment in spinel-bearing calcium-aluminium-rich inclusions among L-type asteroids. *Icarus* 304, 31–57. doi:10.1016/j.icarus.2017.12.026, arXiv:1802.06975.
- W. Freudling et al., 2013. Automated data reduction workflows for astronomy. The ESO Reflex environment. *A&A* 559, A96. doi:10.1051/0004-6361/201322494, arXiv:1311.5411.
- M. J. Gaffey, J. F. Bell, R. H. Brown, T. H. Burbine, J. L. Piatek, K. L. Reed and D. A. Chaky, 1993. Mineralogical variations within the S-type asteroid class. *Icarus* 106, 573–602. doi:10.1006/icar.1993.1194.
- R. Gilmozzi and J. Spyromilio, 2008. The 42m European ELT: status. volume 7012 of *Society of Photo-Optical Instrumentation Engineers (SPIE) Conference Series*. p. 701219. doi:10.1117/12.790801.
- B. J. Gladman, J. A. Burns, M. Duncan, P. Lee and H. F. Levison, 1996. The exchange of impact ejecta between terrestrial planets. *Science* 271, 1387–1392. doi:10.1126/science.271.5254.1387.
- B. J. Gladman, J. A. Burns, M. J. Duncan and H. F. Levison, 1995. The dynamical evolution of lunar impact ejecta. *Icarus* 118, 302–321. doi:10.1006/icar.1995.1193.
- B. Hapke, 1981. Bidirectional reflectance spectroscopy. I - Theory. *Journal of Geophysical Research (Solid Earth)* 86, 3039–3054. doi:10.1029/JB086iB04p03039.
- B. Hapke, 1984. Bidirectional reflectance spectroscopy 3. Correction for macroscopic roughness. *Icarus* 59, 41–59. doi:10.1016/0019-1035(84)90054-X.
- B. Hapke, 1986. Bidirectional reflectance spectroscopy 4. The extinction coefficient and the opposition effect. *Icarus* 67, 264–280. doi:10.1016/0019-1035(86)90108-9.
- B. Hapke, 2001. Space weathering from Mercury to the asteroid belt. *Journal of Geophysical Research (Planets)* 106, 10039–10074. doi:10.1029/2000JE001338.
- J. Hardorp, 1978. The sun among the stars. I. A search for solar spectral analogs. *A&A* 63, 383–390.
- W. K. Hartmann and D. R. Davis, 1975. Satellite-Sized Planetesimals and Lunar Origin. *Icarus* 24, 504–515. doi:10.1016/0019-1035(75)90070-6.
- W. K. Hartmann, G. Ryder, L. Dones and D. Grinspoon, 2000. The time-dependent intense bombardment of the primordial Earth/Moon system. pp. 493–512.
- T. Hiroi and S. Sasaki, 2001. Importance of space weathering simulation products in compositional modeling of asteroids: 349 Dembowska and 446 Aeternitas as examples. *Meteoritics and Planetary Science* 36, 1587–1596. doi:10.1111/j.1945-5100.2001.tb01850.x.
- B. H. N. Horgan, E. A. Cloutis, P. Mann and J. F. Bell, 2014. Near-infrared spectra of ferrous mineral mixtures and methods for their identification in planetary surface spectra. *Icarus* 234, 132–154. doi:10.1016/j.icarus.2014.02.031.
- Ž. Ivezić et al., 2019. LSST: From science drivers to reference design and anticipated data products. *ApJ* 873, 111. doi:10.3847/1538-4357/ab042c, arXiv:0805.2366.
- H. M. Kaluna, H. A. Ishii, J. P. Bradley, J. J. Gillis-Davis and P. G. Lucey, 2017. Simulated space weathering of Fe- and Mg-rich aqueously altered minerals using pulsed laser irradiation. *Icarus* 292, 245–258. doi:10.1016/j.icarus.2016.12.028, arXiv:1612.09396.
- R. L. Klima et al., 2011. New insights into lunar petrology: Distribution and composition of prominent low-Ca pyroxene exposures as observed by the Moon Mineralogy Mapper (M³). *Journal of Geophysical Research (Planets)* 116, 1–13. doi:10.1029/2010JE003719.
- T. Kohout et al., 2014. Space weathering simulations through controlled growth of iron nanoparticles on olivine. *Icarus* 237, 75–83. doi:10.1016/j.icarus.2014.04.004, arXiv:1404.2956.
- A. U. Landolt, 1983. UBVR photometric standard stars around the celestial equator. *AJ* 88, 439–460. doi:10.1086/113329.

- L. F. Lim, J. P. Emery, M. Mueller, A. S. Rivkin, D. Trilling and B. J. Burt, 2011. Olivine composition of the Mars Trojan 5261 Eureka: Spitzer IRS data, in: EPSC-DPS Joint Meeting 2011, p. 1199.
- M. P. Lucas, J. P. Emery, N. Pinilla-Alonso, S. S. Linday and V. Lorenzi, 2017. Hungaria Asteroid Region Telescopic Spectral Survey (HARTSS) I: Stony asteroids abundant in the Hungaria background population. *Icarus* 291, 268–287. doi:10.1016/j.icarus.2016.11.002.
- N. E. Marks, L. E. Borg, C. K. Shearer and W. S. Cassata, 2019. Geochronology of an Apollo 16 clast provides evidence for a basin-forming impact 4.3 billion years ago. *Journal of Geophysical Research (Planets)* 124, 2465–2481. doi:10.1029/2019JE005966.
- J. R. Masiero, T. Grav, A. K. Mainzer, C. R. Nugent, J. M. Bauer, R. Stevenson and S. Sonnett, 2014. Main-belt Asteroids with WISE/NEOWISE: Near-infrared Albedos. *ApJ* 791, 121. doi:10.1088/0004-637X/791/2/121, arXiv:1406.6645.
- T. B. McCord, R. N. Clark, B. R. Hawke, L. A. McFadden, P. D. Owensby, C. M. Pieters and J. B. Adams, 1981. Moon: near-infrared spectral reflectance, a first good look. *Journal of Geophysical Research* 86, 10883–10892. doi:10.1029/JB086iB11p10883.
- T. J. McCoy, L. R. Nittler, T. H. Burbine, J. I. Trombka, P. E. Clark and M. E. Murphy, 2000. Anatomy of a partially differentiated asteroid: A “NEAR”-sighted view of acapulcoites and lodranites. *Icarus* 148, 29–36. doi:10.1006/icar.2000.6494.
- H. J. Melosh, 1984. Impact ejection, spallation, and the origin of meteorites. *Icarus* 59, 234–260. doi:10.1016/0019-1035(84)90026-5.
- F. Migliorini, P. Michel, A. Morbidelli, D. Nesvorný and V. Zappala, 1998. Origin of Multikilometer Earth- and Mars-Crossing Asteroids: A Quantitative Simulation. *Science* 281, 2022. doi:10.1126/science.281.5385.2022.
- J. Moré, 1978. The levenberg-marquardt algorithm: Implementation and theory, in: G. Watson (Ed.), *Numerical Analysis*. Springer Berlin Heidelberg. volume 630 of *Lecture Notes in Mathematics*, pp. 105–116. URL: <http://dx.doi.org/10.1007/BFb0067700>, doi:10.1007/BFb0067700.
- C. D. Murray and S. F. Dermott, 1999. *Solar system dynamics*.
- J. F. Mustard et al., 2005. Olivine and Pyroxene diversity in the crust of Mars. *Science* 307, 1594–1597. doi:10.1126/science.1109098.
- D. A. Nedelcu et al., 2007. Near infra-red spectroscopy of the asteroid 21 Lutetia. II. Rotationally resolved spectroscopy of the surface. *A&A* 470, 1157–1164. doi:doi.org/10.1051/0004-6361:20066944.
- G. A. Neumann et al., 2015. Lunar impact basins revealed by Gravity Recovery and Interior Laboratory measurements. *Science Advances* 1, e1500852–e1500852. doi:10.1126/sciadv.1500852.
- W. Neumann et al., 2018. Modeling the evolution of the parent body of acapulcoites and lodranites: A case study for partially differentiated asteroids. *Icarus* 311, 146–169. doi:10.1016/j.icarus.2018.03.024.
- D. Perna et al., 2018. A spectroscopic survey of the small near-Earth asteroid population: Peculiar taxonomic distribution and phase reddening. *Planetary and Space Science* 158, 82–95. doi:10.1016/j.pss.2018.03.008.
- C. M. Pieters, 1986. Composition of the lunar highland crust from near-infrared spectroscopy. *Reviews of Geophysics* 24, 557–578. doi:10.1029/RG024i003p00557.
- D. Polishook, S. A. Jacobson, A. Morbidelli and O. Aharonson, 2017. A Martian origin for the Mars Trojan asteroids. *Nature Astronomy* 1, 1–5. doi:10.1038/s41550-017-0179, arXiv:1710.00024.
- M. Popescu, M. Birlan and D. A. Nedelcu, 2012. Modeling of asteroid spectra - M4AST. *A&A* 544, 1–10. doi:10.1051/0004-6361/201219584.
- V. Reddy, T. L. Dunn, C. A. Thomas, N. A. Moskovitz and T. H. Burbine, 2015. Mineralogy and surface composition of asteroids. pp. 43–63. doi:10.2458/azu_uapress_9780816532131-ch003.
- L. Riu, F. Poulet, J. P. Bibring and B. Gondet, 2019. The M³ project: 2 - Global distributions of mafic mineral abundances on Mars. *Icarus* 322, 31–53. doi:10.1016/j.icarus.2019.01.002.
- A. S. Rivkin, R. P. Binzel, E. S. Howell, S. J. Bus and J. A. Grier, 2003. Spectroscopy and photometry of Mars Trojans. *Icarus* 165, 349–354. doi:10.1016/S0019-1035(03)00211-2.
- A. S. Rivkin, F. Marchis, J. A. Stansberry, D. Takir, C. Thomas and the JWST Asteroids focus group, 2016. Asteroids and the James Webb Space Telescope. *PASP* 128, 18003. doi:10.1088/1538-3873/128/959/018003.
- A. S. Rivkin, D. E. Trilling, C. A. Thomas, F. DeMeo, T. B. Spahr and R. P. Binzel, 2007. Composition of the L5 Mars Trojans: Neighbors, not siblings. *Icarus* 192, 434–441. doi:10.1016/j.icarus.2007.06.026, arXiv:0709.1925.
- M. Rodrigues et al., 2018. The HARMONI/ELT spectrographs, in: C. J. Evans, L. Simard and H. Takami (Eds.), *Ground-based and Airborne Instrumentation for Astronomy VII*, International Society for Optics and Photonics. SPIE. pp. 2991–3000. doi:10.1117/12.2313396.
- J. A. Sanchez et al., 2014. Olivine-dominated asteroids: Mineralogy and origin. *Icarus* 228, 288–300. doi:10.1016/j.icarus.2013.10.006, arXiv:1310.1080.
- J. A. Sanchez, V. Reddy, A. Nathues, E. A. Cloutis, P. Mann and H. Hiesinger, 2012. Phase reddening on near-Earth asteroids: Implications for mineralogical analysis, space weathering and taxonomic classification. *Icarus* 220, 36–50. doi:10.1016/j.icarus.2012.04.008, arXiv:1205.0248.
- S. Sasaki, K. Nakamura, Y. Hamabe, E. Kurahashi and T. Hiroi, 2001a. A successful simulation of space weathering – spectral change and nanophase Fe particles on olivine by pulse-laser irradiation, in: *Lunar and Planetary Science Conference*, p. 1610.
- S. Sasaki, K. Nakamura, Y. Hamabe, E. Kurahashi and T. Hiroi, 2001b. Production of iron nanoparticles by laser irradiation in a simulation of lunar-like space weathering. *Nature* 410, 555–557. doi:10.1038/35069013.
- H. Scholl, F. Marzari and P. Tricarico, 2005. Dynamics of Mars Trojans. *Icarus* 175, 397–408. doi:10.1016/j.icarus.2005.01.018.
- J. M. Sunshine, S. J. Bus, T. J. McCoy, T. H. Burbine, C. M. Corrigan and R. P. Binzel, 2004. High-calcium pyroxene as an indicator of igneous differentiation in asteroids and meteorites. *Meteoritics and Planetary Science* 39, 1343–1357. doi:10.1111/j.1945-5100.2004.tb00950.x.
- J. M. Sunshine and C. M. Pieters, 1998. Determining the composition of olivine from reflectance spectroscopy. *Journal of Geophysical Research* 103, 13675–13688. doi:10.1029/98JE01217.
- E. F. Tedesco, P. V. Noah, M. Noah and S. D. Price, 2004. IRAS Minor Planet Survey V6.0. NASA Planetary Data System, IRAS–A–FPA–3–RDR–IMPS–V6.0.
- F. Tera, D. A. Papanastassiou and G. J. Wasserburg, 1974. Isotopic evidence for a terminal lunar cataclysm. *Earth and Planetary Science Letters* 22, 1–21. doi:10.1016/0012-821X(74)90059-4.

- D. E. Trilling, A. S. Rivkin, J. A. Stansberry, T. B. Spahr, R. A. Crudo and J. K. Davies, 2007. Albedos and diameters of three Mars Trojan asteroids. *Icarus* 192, 442–447. doi:10.1016/j.icarus.2007.08.002, arXiv:0709.1921.
- R. P. van der Marel and M. Franx, 1993. A New Method for the Identification of Non-Gaussian Line Profiles in Elliptical galaxies. *ApJ* 407, 525. doi:10.1086/172534.
- J. Vernet et al., 2011. X-shooter, the new wide band intermediate resolution spectrograph at the ESO Very Large Telescope. *A&A* 536, A105. doi:10.1051/0004-6361/201117752, arXiv:1110.1944.
- K. Wickhusen, J. Oberst, K. Willner and A. Christou, 2017. Missions to Mars and his trojan asteroid family - a feasibility study, in: European Planetary Science Congress, pp. EPSC2017–322.
- M. Yamada et al., 1999. Simulation of space weathering of planet-forming materials: Nanosecond pulse laser irradiation and proton implantation on olivine and pyroxene samples. *Earth, Planets, and Space* 51, 1265. doi:10.1186/BF03351599.
- M. Yoshikawa, J. Kawaguchi, A. Fujiwara and A. Tsuchiyama, 2015. Hayabusa sample return mission. pp. 397–418. doi:10.2458/azu_uapress_9780816532131-ch021.
- Y.-L. Zou, J.-Z. Liu, J.-J. Liu and T. Xu, 2004. Reflectance spectral characteristics of lunar surface materials. *ChJAA* 4, 97–104. doi:10.1088/1009-9271/4/1/97.
- M. T. Zuber, 2001. The crust and mantle of Mars. *Nature* 412, 220–227. doi:10.1038/35084163.